Multielectron effects and nonadiabatic electronic dynamics in above threshold ionization and high-harmonic generation

2011 New J. Phys. 13 093010

(http://iopscience.iop.org/1367-2630/13/9/093010)

New Journal of Physics
The open-access journal for physics

Multielectron effects and nonadiabatic electronic dynamics in above threshold ionization and high-harmonic generation

Michael Spanner[1,3], Jochen Mikosch[1], Arjan Gijsbertsen[1,2], Andrey E Boguslavskiy[1] and Albert Stolow[1]

[1] Steacie Institute for Molecular Sciences, National Research Council of Canada, Ottawa, ON, K1A 0R6, Canada
[2] FOM instituut voor atoom- en molecuulfysica (AMOLF), Science Park 102, 1098 XG Amsterdam, The Netherlands
E-mail: michael.spanner@nrc.ca

New Journal of Physics **13** (2011) 093010 (17pp)
Received 9 May 2011
Published 7 September 2011
Online at http://www.njp.org/
doi:10.1088/1367-2630/13/9/093010

Abstract. We explore the effects of multiple participating final ion states during strong field ionization (SFI) and high-harmonic generation (HHG) using a two-electron two-center reduced-dimensionality model. In particular, we propose to use above threshold ionization (ATI) photoelectron spectra to identify ionic states that are active in SFI, and demonstrate the feasibility of our proposal to track multiple ionic states in a dissociation scenario. In addition to offering clear signatures of multiple participating ionic states, our method is shown to be sensitive to sub-cycle nonadiabatic laser-driven couplings between the ionic states. Finally, we calculate the high-harmonic emission and show how the multiple ionic states identified in the ATI spectra can manifest themselves in the high-harmonic spectra.

[3] Author to whom any correspondence should be addressed.

Contents

1. Introduction

The dynamics of molecules consists of the motion of the constituent atoms, the valence electrons that bind them and the coupling between the two. Just as femtosecond science is currently used to follow the movements of atoms within a molecule, attosecond science [1], which derives from the high-harmonic generation (HHG) process [2], promises to do the same for electrons. Within the standard single active electron (SAE) model [2], HHG involves the adiabatic strong field ionization (SFI) of a bound electron from the highest occupied molecular orbital (HOMO), propagation and acceleration of the liberated electron in the laser field, and recombination of the electron with the parent ion to produce harmonic radiation. From this perspective, HHG incorporates only the ground state of the ion following ionization. However, recent theory and experiments have begun to see the influence of multiple final ion states in HHG and SFI [3–6], a fundamentally multi-electron effect as it relies on the presence of at least one continuum and one bound ionic electron. These works offer indirect evidence for multiple active ionic states as interpretation relies on the accurate and careful modeling of the HHG signal.

In SFI, there are several mechanisms that can populate excited final ion states. Firstly, the ionizing system can make a transition directly from the neutral to excited final ion states [3–6]. Within a Hartree–Fock picture this means that ionization can occur from lower-lying occupied orbitals (HOMO-1, HOMO-2, etc) and not just from the HOMO. Secondly, a continuum electron born from the HOMO can excite the ground state of the ion upon recollision [7]. Finally, nonadiabatic laser-driven excitations [8] in the ion can occur following ionization. Since HHG is fundamentally a sub-cycle process, this last mechanism can affect it only if the nonadiabatic ionic transitions occur on a sub-cycle timescale [9].

In this paper, we explore a direct method for probing the influence of multiple final ionic states in strong field dynamics using above threshold ionization (ATI). ATI is a strong field process where an atom or molecule is ionized by absorbing more than the minimum number of photons required. The resulting photoelectron kinetic energy spectra show a series of peaks with spacing equal to the photon energy. The positions of the ATI photoelectron peaks as a function

of the photoelectron kinetic energy are given as [10]

$$E_{\rm kin} = \frac{p^2}{2} = n\omega - (I_{\rm p} + U_{\rm p}), \tag{1}$$

where $I_{\rm p}$ is the ionization potential of the target, and $U_{\rm p} = F_0^2/(4\omega^2)$ is the pondermotive potential, which corresponds to the average energy gained by the liberated electron oscillating freely in the laser field. Here F_0 and ω are the peak electric field strength and frequency of the ionizing laser. If multiple final ionic states do participate in SFI processes, then there must be evidence for these multiple states in the photoelectron ATI spectra. In particular, one would expect to see more than one series of ATI peaks, with each series carrying a different $I_{\rm p}$ shift.

Our ATI probing method is illustrated using a two-electron reduced-dimensionality model that permits full numerical solution of both the ATI and HHG spectra. We find that multiple final ion states are indeed populated in this system during SFI, and that the ATI photoelectron reveals the presence of multiple active ionic states. The dominant mechanisms leading to excited ionic states in our model system are recollision excitation at small bond lengths and sub-cycle nonadiabatic laser-driven couplings at large bond lengths. We find that ionic-state-resolved ATI spectra carry information about sub-laser-cycle nonadiabatic electronic dynamics, and can thus be used to distinguish adiabatic from nonadiabatic excitation mechanisms, both leading to excited ionic population. Although the scope of this paper is limited to a theoretical investigation, the probing of multiple ionic states via ATI has been successfully implemented in recent experiments on 1,3-butadiene and butane, revealing direct sub-cycle ionization to multiple final ionic states in these molecules [11].

2. Methodology

2.1. Model system

In the spirit of the 'Eberlonium' models [12], a series of reduced-dimensionality models often used in strong field physics, we work with a two-electron two-center system with each electron moving in a single dimension. Although we calculate ATI and HHG spectra for a range of bond lengths, thus enabling an investigation of a two-center dissociation scenario, we solve only the electronic part of the problem assuming perfect Born–Oppenheimer separation of the nuclear and electronic degrees of freedom. We consider the singlet case where the two-electron spins are opposite, and hence we use symmetric spatial wavefunctions only. The two-electron Hamiltonian of the neutral system is given by

$$H^{\rm N}(x_1, x_2, t) = -\frac{1}{2}\frac{\partial^2}{\partial x_1^2} - \frac{1}{2}\frac{\partial^2}{\partial x_2^2} + V_n(x_1) + V_n(x_2) + V_{ee}(x_1 - x_2) - F(t)(x_1 + x_2), \tag{2}$$

where

$$V_{ee}(x_1 - x_2) = \frac{1}{\sqrt{(x_1 - x_2)^2 + b^2}} \tag{3}$$

is the electron–electron interaction,

$$V_n(x) = -\frac{1}{\sqrt{(x + R/2)^2 + a^2}} - \frac{1}{\sqrt{(x - R/2)^2 + a^2}} \tag{4}$$

is the nuclear two-center binding potential, $F(t)$ is the electric field of the laser and R is the bond length. The single-electron Hamiltonian describing the ion is given by

$$H^{\mathrm{I}}(x_1, t) = -\frac{1}{2}\frac{\partial^2}{\partial x_1^2} + V_n(x_1) - F(t)x_1. \tag{5}$$

(Note that due to antisymmetrization of electrons, the labels x_1 and x_2 are interchangeable.) Below we solve the time-dependent Schrödinger equation for this Hamiltonian numerically using the Fourier split-operator method to find the time-dependent two-electron wavefunction $\Psi(x_1, x_2, t)$. Bound states are found by propagating a suitable initial guess for the states in complex time.

In the following, we pick the values of $a = 0.8$ and $b = 0.8$ for the soft-core potentials. The energies of the neutral ground state and the lowest two ionic states of this system as a function of the bond length R are plotted in the top panels of figure 1. Both field-free and cycle-averaged laser-dressed energies are shown (see the following section for the definition of the laser-dressed states). The bottom panels show the bond-dependent ionization potentials from the neutral ground state to the lowest two ionic states. Note that there is nothing particularly special about our choice of soft-core parameters other than that they lead to qualitatively realistic potential energy surfaces. All features common to diatomics, for example bonding/anti-bonding states and bond-dependent vertical ionization potentials, are present.

We investigate this reduced-dimensionality model as it permits full numerical solution of the exact quantum dynamics; thus all effects discussed are in this sense real quantum effects that could occur in real molecular systems. Although our model could be interpreted as a one-dimensional (1D) version of H_2, we would hesitate to put forth this perspective. While the range of mechanisms and phenomena discussed below undoubtedly occur to some extent in real H_2, we in no way suggest that the present results quantitatively reproduce 3D H_2. First, since our nuclei are frozen, no influence of nuclear dynamics is present. Some obvious effects to expect are broadening of the ATI peaks due to multiple possible vibrational transitions to the ionic state governed (at least partially) by Frank–Condon factors. Due to the discrete nature of the vibrational transitions, one could perhaps expect a less continuous shifting of the ATI peak positions (as shown and discussed below in figure 2) when the continuous scanning of the bond length is replaced by a real vibrational wave packet that accounts for discrete transitions. As is typical of this series of reduced-dimensionality models [12], the one-dimensional (1D) nature leads to a larger recollision probability as compared to a 3D system since the continuum wave packet cannot spread in the transverse directions. Further, 1D systems typically exhibit larger polarizabilities than their 3D counterparts. However, since full-dimensionality simulations that include moving nuclei coupled to 3D multielectron dynamics are not currently computationally feasible, the present reduced-dimensionality model presents a valuable conceptual tool or 'springbroad' to start studying the multielectron effects expected to arise in strong field molecular experiments.

2.2. Expansion of the complete wavefunction into laser-dressed neutral and ionic states

We are interested in understanding the contribution to ATI and HHG arising from multiple ionic states. Analysis of the ATI photoelectrons is done after the laser pulse. In this case, the part of the wavefunction corresponding to single ionization (one electron near the core and the other

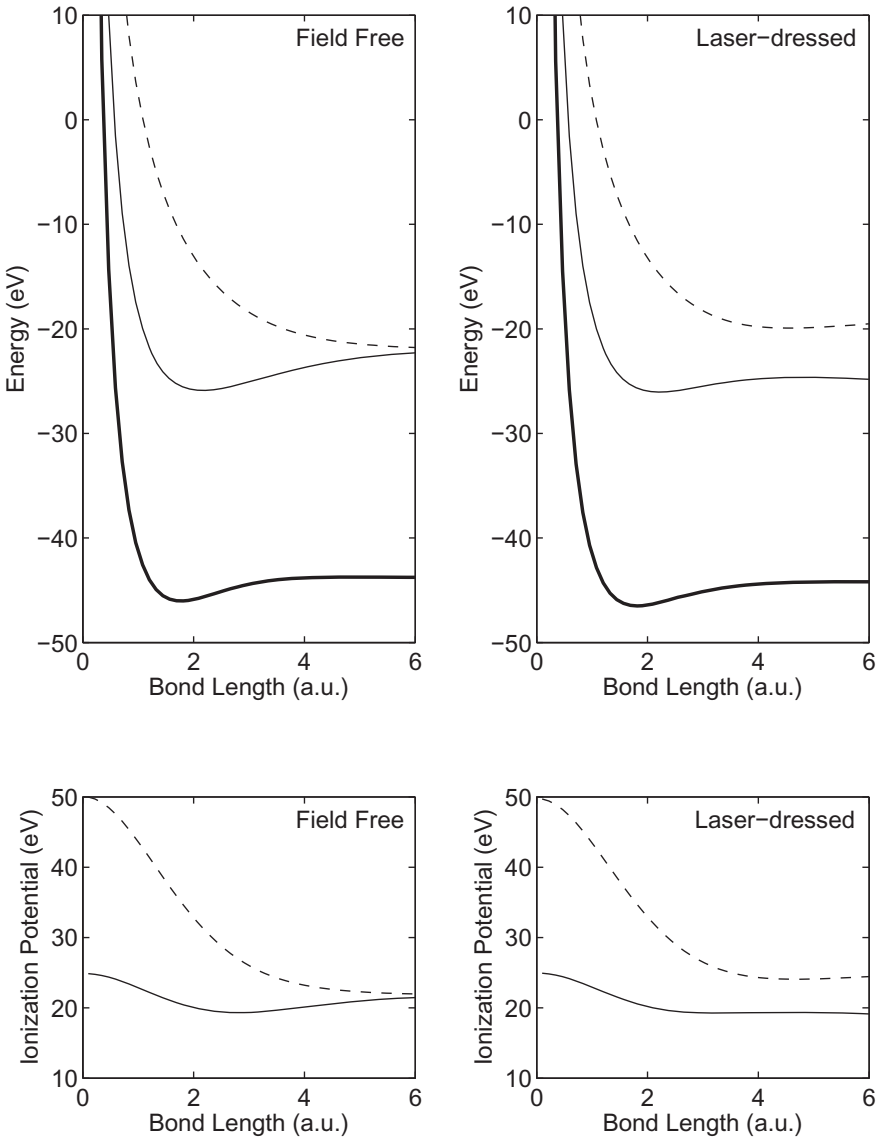

Figure 1. Top: field-free and (cycle-averaged) laser-dressed potential energy curves for the neutral groundstate (thick solid), ionic groundstate (thin solid) and first excited ionic state (dashed). Bottom: ionization potentials from the neutral groundstate to the ionic groundstate (solid) and to the first excited ionic state (dashed).

electron far from the core) can be decomposed using the field-free ionic states (eigenstates of H^{I}). HHG emission, on the other hand, occurs while the field is present. In order to quantify and disentangle the contributions to HHG arising from multiple ionic states, we choose to decompose the complete two-electron wavefunction $\Psi(x_1, x_2, t)$ into adiabatic laser-dressed neutral and ionic states. We now outline the procedure used to achieve this decomposition.

The lowest few field-free neutral bound states $\phi_j^{\mathrm{N}}(x_1, x_2)$ and ionic bound states $\phi_j^{\mathrm{I}}(x_1)$ are computed by solving the corresponding field-free eigenvalue problems ($F(t) = 0$ in

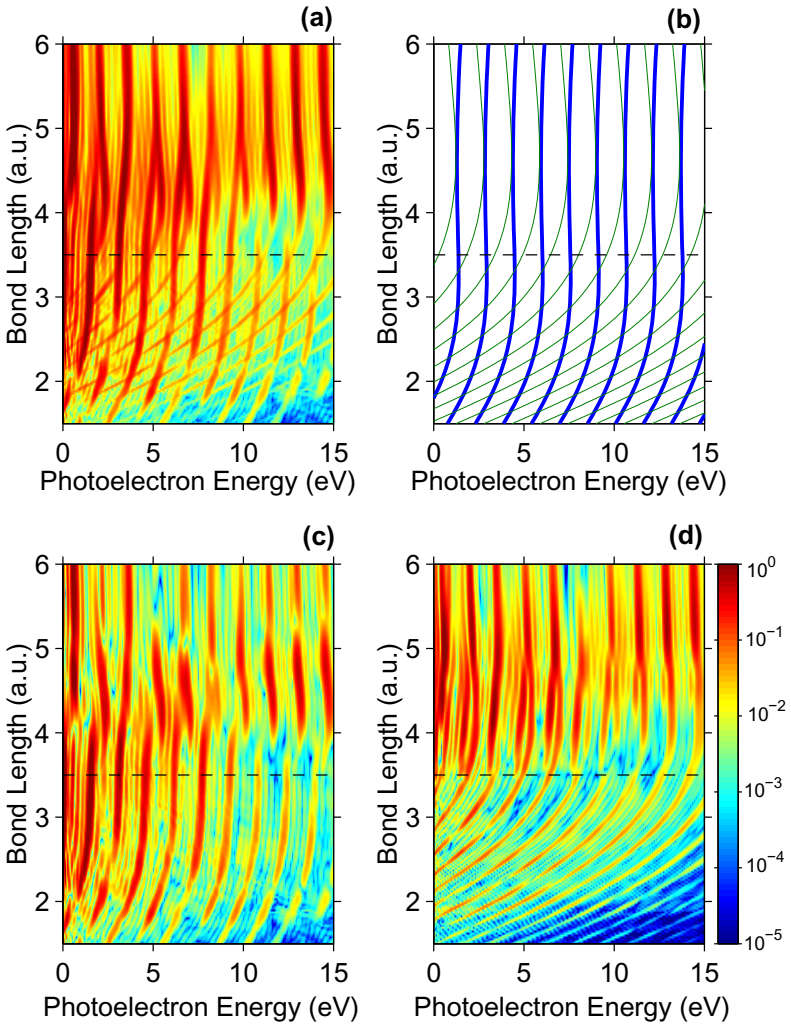

Figure 2. ATI photoelectron spectra as a function of bond length. (a) Two series of ATI peaks can be seen in the total ATI signal. Panel (b) plots the expected ATI peak positions using equation (1) and the time-averaged dressed-state ionization potentials. Panels (c) and (d) show the channel-resolved ATI spectra corresponding to the ground and excited ionic channels, respectively. The dashed line in all plots at $R_0 = 3.5$ a.u. denotes a characteristic bond length at which a qualitative change in behavior of the total and channel-resolved ATI spectra is manifest (see text).

equations (2) and (5)) for the neutral and ionic states, respectively,

$$H^{\mathrm{N}}(x_1, x_2)\phi_j^{\mathrm{N}}(x_1, x_2) = E_j^{\mathrm{N}}\phi_j^{\mathrm{N}}(x_1, x_2), \tag{6a}$$

$$H^{\mathrm{I}}(x_1)\phi_j^{\mathrm{I}}(x_1) = E_j^{\mathrm{I}}\phi_j^{\mathrm{I}}(x_1). \tag{6b}$$

In the results below, we included the lowest four states of the neutral and the lowest six states of the ion in our bound state basis. Next, the adiabatic laser-dressed states are found by diagonalizing the corresponding laser-dressed Hamiltonian expanded in the basis of the chosen

field-free states at each time t

$$\begin{bmatrix} E_0^{(k)}+d_{00}^{(k)} & d_{01}^{(k)} & d_{02}^{(k)} & \\ d_{10}^{(k)} & E_1^{(k)}+d_{11}^{(k)} & d_{12}^{(k)} & \cdots \\ d_{20}^{(k)} & d_{21}^{(k)} & E_2^{(k)}+d_{22}^{(k)} & \\ & \vdots & & \ddots \end{bmatrix} \begin{bmatrix} c_{0,m}^{(k)} \\ c_{1,m}^{(k)} \\ c_{2,m}^{(k)} \\ \vdots \end{bmatrix} = E_m^{(k),LD} \begin{bmatrix} c_{0,m}^{(k)} \\ c_{1,m}^{(k)} \\ c_{2,m}^{(k)} \\ \vdots \end{bmatrix}, \tag{7}$$

where $k = \mathrm{N}, \mathrm{I}$ denotes either the neutral (N) or ionic (I) space, $E_m^{(k),\mathrm{LD}}$ is the laser-dressed energy of the state m, and $\mathrm{d}_{nm}^N = -\langle\phi_n^{(k)}|F(t)(x_1+x_2)|\phi_m^{(k)}\rangle$ and $\mathrm{d}_{nm}^I = -\langle\phi_n^{(k)}|F(t)x_1|\phi_m^{(k)}\rangle$ account for the laser coupling between the field-free states. The position representations of the laser-dressed neutral and ionic states, which are now dependent parametrically on the instantaneous value of the field $F(t)$ through the coefficients $c_{n,m}^{(k)}$, are then given by

$$\phi_m^{\mathrm{N,LD}}(x_1, x_2;\, F(t)) = \sum_n c_{n,m}^N(F(t))\phi_n^{\mathrm{N}}(x_1, x_2), \tag{8a}$$

$$\phi_m^{\mathrm{I,LD}}(x_1;\, F(t)) = \sum_n c_{n,m}^I(F(t))\phi_n^{\mathrm{I}}(x_1). \tag{8b}$$

With the laser-dressed states in hand, we can proceed with the decomposition of the full wavefunction $\Psi(x_1, x_2, t)$ into neutral, ionic and continuum components. We first calculate the projections onto the laser-dressed neutral states

$$A_m^{\mathrm{N,LD}}(t) = \langle\phi_m^{\mathrm{N,LD}}(x_1, x_2;\, F(t))|\Psi(x_1, x_2, t)\rangle \tag{9}$$

and project them out of the full wavefunction to give

$$\Psi'(x_1, x_2, t) = \Psi(x_1, x_2, t) - \sum_m A_m^{\mathrm{N,LD}}(t)\phi_m^{\mathrm{N,LD}}(x_1, x_2;\, F(t)). \tag{10}$$

$\Psi'(x_1, x_2, t)$ now contains only the ionic and continuum contributions. We decompose $\Psi'(x_1, x_2, t)$ into the form

$$\Psi'(x_1, x_2, t) = \sum_m [\phi_m^{\mathrm{I,LD}}(x_1;\, F(t))\chi_m(x_2, t) + \chi_m(x_1, t)\phi_m^{\mathrm{I,LD}}(x_2;\, F(t))], \tag{11}$$

which represents the symmetrized sum of all states containing one bound ionic electron and one continuum electron. The continuum functions $\chi_m(x_2, t)$ in this expansion are found by first projecting $\Psi'(x_1, x_2, t)$ onto the state $\phi_m^{\mathrm{I,LD}}(x_1;\, F(t))$ and then applying the projector

$$\hat{P} = 1 - \frac{1}{2}\sum_m |\phi_m^{\mathrm{I,LD}}(x_2;\, F(t))\rangle\langle\phi_m^{\mathrm{I,LD}}(x_2;\, F(t))| \tag{12}$$

to the result to avoid overcounting the bound component [7]

$$|\chi_m(x_2, t)\rangle = \hat{P}\langle\phi_m^{\mathrm{I,LD}}(x_1;\, F(t))|\Psi'(x_1, x_2, t)\rangle. \tag{13}$$

The full wavefunction $\Psi(x_1, x_2, t)$ is then written in terms of the neutral, ionic and continuum components as

$$\Psi(x_1, x_2, t) \approx \sum_n A_n^{\mathrm{N,LD}}(t)\phi_n^{\mathrm{N,LD}}(x_1, x_2;\, F(t)) + \sum_m [\phi_m^{\mathrm{I,LD}}(x_1;\, F(t))\chi_m(x_2, t) + \chi_m(x_1, t)\phi_m^{\mathrm{I,LD}}(x_2;\, F(t))] \equiv \Psi^{\mathrm{ex}}(x_1, x_2, t). \tag{14}$$

Two points should be emphasized. Firstly, the expansion $\Psi^{\mathrm{ex}}(x_1, x_2, t)$ is simply a convenient way to analyze the full wavefunction $\Psi(x_1, x_2, t)$, but it is not used to actually propagate the full wavefunction. Propagation of the full system to find $\Psi(x_1, x_2, t)$ is always done using a 2D Cartesian grid. Secondly, when using the expansion $\Psi^{\mathrm{ex}}(x_1, x_2, t)$ in the analysis below, we explicitly exclude contributions where both electrons are simultaneously in continuum states; the possibility of double ionization is completely neglected in the definition of $\Psi^{\mathrm{ex}}(x_1, x_2, t)$.

2.3. Signatures of multiple final ionic states in high-harmonic generation (HHG)

We calculate the full harmonic emission using the dipole acceleration

$$\begin{aligned}\ddot{\mathrm{d}}(t) &= \frac{\mathrm{d}^2}{\mathrm{d}t^2}\left\langle \sum_{i=1,2} x_i \right\rangle \\ &= \langle \Psi(x_1, x_2, t)|a_e(x_1, x_2)|\Psi(x_1, x_2, t)\rangle,\end{aligned} \tag{15}$$

where

$$a_e(x_1, x_2) = \sum_{i=1,2} \frac{\partial V(x_1, x_2)}{\partial x_i} \tag{16}$$

is the electronic acceleration operator,

$$V(x_1, x_2) = V_n(x_1) + V_n(x_2) + V_{ee}(x_1 - x_2) - F(t)(x_1 + x_2) \tag{17}$$

is the potential energy of the system, and Ehrenfest's theorem is used [13] for the last step in equation (15). The harmonic spectrum is then obtained by Fourier transforming the dipole acceleration

$$S_{hhg}(\omega) = \int \mathrm{e}^{\mathrm{i}\,\omega t}\ddot{\mathrm{d}}(t)\mathrm{d}t. \tag{18}$$

This yields the full harmonic spectrum that includes contributions from all possible ionic states.

In order to assess the contribution to the HHG signal originating from specific intermediate ionic states, we also calculate the dipole acceleration using the expansion $\Psi^{\mathrm{ex}}(x_1, x_2, t)$ and neglect continuum–continuum as well as bound–bound contributions to give

$$\ddot{\mathrm{d}}^{\mathrm{ex}}(t) = \sum_{nm} \ddot{\mathrm{d}}^{\mathrm{ex}}_{nm}(t), \tag{19}$$

where

$$\ddot{\mathrm{d}}^{\mathrm{ex}}_{nm}(t) = 2(A_n^{\mathrm{N,LD}}(t))^*\langle \phi_n^{\mathrm{N,LD}}(x_1, x_2;\, F(t))|a_e(x_1, x_2)|\phi_m^{\mathrm{I,LD}}(x_1;\, F(t)),\, \chi_m(x_2, t)\rangle + \mathrm{c.c.} \tag{20}$$

represents recombination from the continuum electron $\chi_m(x_2, t)$ to the neutral bound state $\phi_n^{\mathrm{N,LD}}(x_1, x_2;\, F(t))$. The corresponding spectrum $S^{\mathrm{ex}}_{hhg}(\omega)$ is calculated by Fourier transforming $\ddot{\mathrm{d}}^{\mathrm{ex}}(t)$ as in equation (18). For our model system and chosen laser intensities, excitation of neutral excited states was negligible, and hence the sum over the neutral bound states (the sum over n) in expression equation (19) could be truncated to include only the ground state for the present scenario. Written this way, equations (19) and (20) allow us to analyze the total HHG signal in terms of individual ionic channel contributions.

3. Multiple ionic states in the photoelectron above threshold ionization (ATI) spectra

3.1. ATI spectra

We now consider the ATI spectra of the two-electron model. The electric field of the laser is written as

$$F(t) = F_0 f(t) \sin(\omega_0 t). \tag{21}$$

We use $\omega_0 = 0.057$ a.u. corresponding to a wavelength of 800 nm and a peak intensity corresponding to 1.5×10^{14} W cm^{-2}. The envelope of the laser pulse was chosen to be a flat-top pulse with $\sin^2$ turn-on and turn-off

$$f(t) = \begin{cases} 0, & t < 0, \\ \sin^2\left(\dfrac{\pi t}{\tau_{\rm on}}\right), & 0 < t < \tau_{\rm on}, \\ 1, & \tau_{\rm on} < t < (\tau_{\rm on} + N\tau), \\ \sin^2\left(\dfrac{\pi(t - N\tau)}{\tau_{\rm on}}\right), & (\tau_{\rm on} + N\tau) < t < (2\tau_{\rm on} + N\tau), \\ 0, & t > (2\tau_{\rm on} + N\tau), \end{cases} \tag{22}$$

where $\tau = 2\pi/\omega_0$ is the period of the carrier frequency, $\tau_{\rm on}$ is the turn on time of the pulse and the flat-top portion of the pulse is N cycles long. In the calculations below, we use a two-cycle turn-on ($\tau_{\rm on} = 2\tau$) and a four-cycle plateau ($N = 4$).

Figure 2 shows the calculated ATI spectra as a function of bond length. At the chosen intensity, negligible double ionization occurs. Panel (a) shows the total ATI spectra. Two combs of ATI peaks are visible, and the two combs display different shifts as the bond length is changed. Panel (b) plots the expected ATI peak positions for the two lowest ionic states according to equation (1) using the time-averaged laser-dressed ionization potentials. Below the bond length of 3.5 a.u. ($\equiv R_0$) denoted by a dashed line, the calculated ATI combs in panel (a) are in excellent agreement with the expected peak positions plotted in panel (b), showing that the two ATI combs originate from ionization to the ground and first excited states of the ion. For bond lengths larger than R_0, the agreement is less pronounced; we will return to this point below. Panels (c) and (d) plot the same ATI spectra but now correlated to the ground and first excited states of the ion, respectively. That is, we use the expansion $\Psi^{\rm ex}(x_1, x_2, t)$ from equation (14), with $F(t) = 0$, to separate the ATI photoelectrons correlated to the ground and first excited states of the ion. This would correspond to measuring the ATI photoelectron in coincidence with the final ion state. Panels (c) and (d) show that the two ATI combs separate cleanly below R_0 when correlated to the final ion state. However, above R_0, the two combs are mixed and cannot be separated, even in correlation with the final ion state. Figure 3 plots the fractional yield of all ATI electrons correlated to the ground (solid line) and excited (dashed line) ionic channels. By fractional yield, we mean the ATI yield to a particular channel divided by the total ATI yield summed over both channels. For small bond lengths, the ATI yields are dominated by the ground state channel, with only about 10% to the first excited state. For large bond lengths, the ATI yield is evenly distributed between the ground and first excited ion channels. This qualitative change in the behavior of the ATI spectra around R_0 suggests a change in the underlying mechanism of populating the excited ionic state. Furthermore, we note that there is no obvious feature in

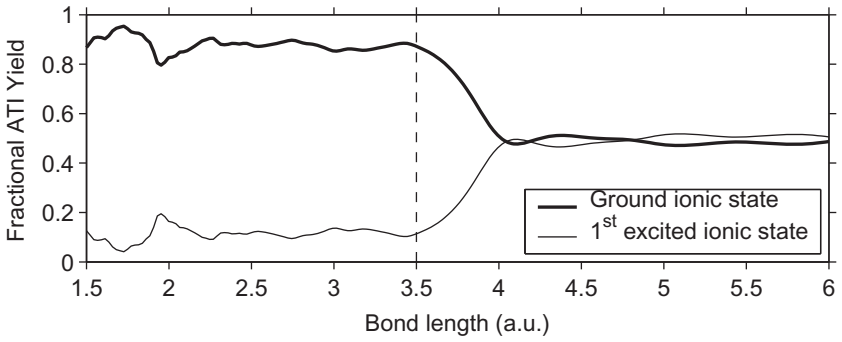

Figure 3. Fractional ATI yield correlated to the ground and first excited ionic states. The dashed line denotes $R_0 = 3.5$ a.u.

the field-free potential energy curve (figure 1), such as a crossing of surfaces, that would signal this behavioral change. As will be discussed below, this change at R_0 is related to the onset of nonadiabatic laser-driven couplings in the ionic states; specifically, it signals the onset of dynamical electron localization [15, 16] in the ion.

3.2. Mechanism at small bond lengths: recollision excitation

We now turn to the mechanisms leading to excited ionic states in our model. Consider the small bond length regime. We first note that at bond lengths smaller than R_0, we have checked that there is effectively no laser-driven excitation of bound neutral dressed states, thus ruling out nonadiabatic laser-driven multielectron excitations (NME) [8] in the neutral as the possible mechanism. Likewise, laser-driven excitation of bound ionic dressed states following ionization does not occur, i.e. no NME in the ion.

Consideration of the sub-cycle ionization and continuum dynamics reveals the operative excitation mechanism. Figure 4 shows plots of the time-dependent continuum wavefunctions correlated to the ground (top) and first excited (bottom) ionic states, $|\chi_0(x_1, t)|^2$ and $|\chi_1(x_1, t)|^2$, respectively, for $R = 1.5$ a.u. In order to focus on the sub-cycle dynamics, these plots were calculated using an instantaneous turn-on at $t = 0$ of the driving laser field. The system was initialized in the neutral ground state. During the first half-cycle, we see substantial ionization to the ground ionic channel and negligible ionization to the first excited ionic channel (less than 1% of the yield to the ground ionic channel, mostly due to the instantaneous turn-on of the driving field). This latter point rules out direct SFI to the first excited ionic states as the mechanism of ionic excitation. During the second half-cycle, as part of the continuum electron correlated to the ground ionic channel recollides with the core, we see a marked increase in the continuum correlated to the first excited ionic channel. This recollision excitation causes about 10% of the continuum population to be transferred from the ground ionic channel to the first excited ionic channel. Thus, at small bond lengths, the dominant mechanism to populate excited ionic states is through recollision excitation, where ionization occurs first to the ground state of the ion during one half-cycle, followed by collisional excitation of the ion during the next half-cycle. The effects of this process on the two-center minimum in HHG [14] were discussed in a recent theoretical paper [7].

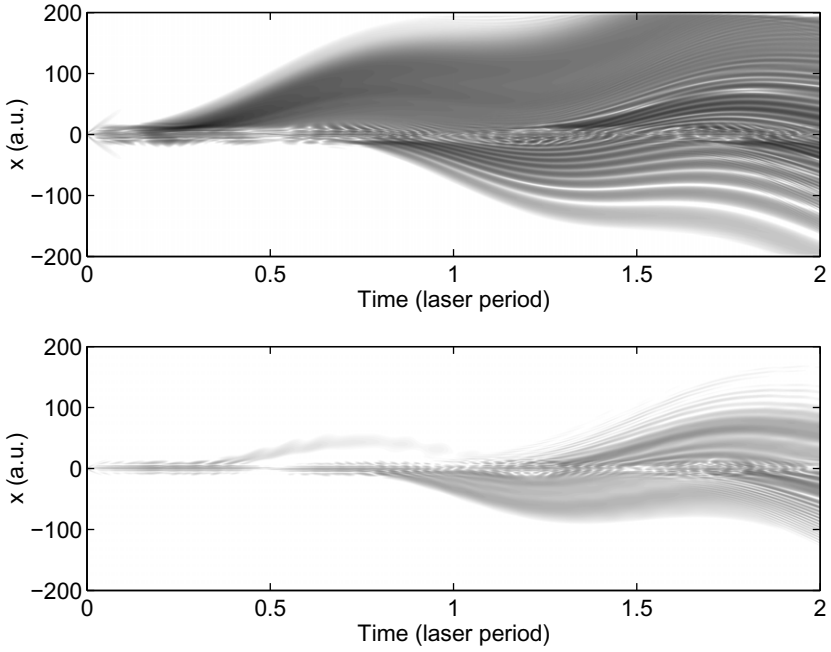

Figure 4. Sub-cycle dynamics of the continuum functions $|\chi_0(x_1, t)|^2$ (top) and $|\chi_1(x_1, t)|^2$ (bottom) correlated to the ground and first excited ionic states, respectively. Bond length $R = 1.5$ a.u. These plots demonstrate the recollision excitation of the first ionic state that occurs around $t = 0.8$–1.1 in units of the laser cycle.

3.3. Mechanism at large bond lengths: electron localization

For bond lengths larger than R_0, a different mechanism emerges. In this regime, strong laser-driven excitation/coupling of the bound ionic states occurs due to the fact that the electronic energy-level gaps decrease as the bond length increases. To demonstrate this point, we simulated the bound ionic dynamics by solving the time-dependent version of equation (7) for the ionic space, with the initial condition that all population is in the ground state of the ion and using the laser pulse given in equation (22). As an indicator of bound state excitation and/or coupling, in figure 5 we plot the time averaged population of the ground and first excited ionic states, for the range of bond lengths considered above. For $R < R_0$, no excitation of the ionic states occurs, as previously stated. However, for $R > R_0$, strong coupling of the ground and first ionic states occurs, and the system on average spends as much time in the excited ionic state as it does in the ground ionic state. Note the strong resemblance between figures 3 and 5; the switch in the behavior of the ATI spectra near $R = R_0$ is linked to the ionic state couplings. It should also be stated that similar plots for the neutral dynamics showed negligible neutral bound state excitation across the whole range of bond lengths.

What is occurring in the large bond length regime is electron localization [15, 16], a particular regime of nonadiabatic bound state dynamics. In our diatomic model at large bond lengths, the adiabatic field-dressed ionic states have their charge distributions localized on either the right or left nucleus. As the electric field of the laser sweeps through zero and changes sign, the ionic charge distribution cannot keep up with the laser oscillations, and gets localized on

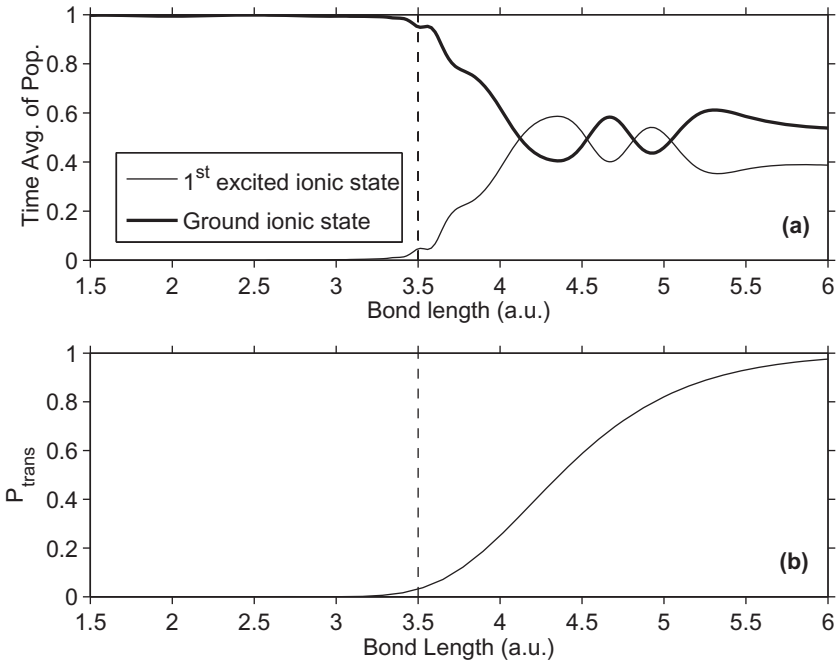

Figure 5. Top: time-averaged (over the pulse duration) populations of the ground and first excited ionic states as a function of bond length. The initial states for these simulation had all populations in the ionic ground state. This plot demonstrates that electron localization in the ion starts to occur for a bond length of ~ 3.5 a.u. ($\equiv R_0$, dashed line) or greater. Bottom: probability for a nonadiabatic transition between the two states during one field zero crossing near the peak of the pulse envelope.

one of the nuclei. In the basis of adiabatically dressed states, this means that there is a rapid transition between the ground and first excited state at every zero crossing of the field. Averaging the state populations over a few cycles thus leads to equal time-averaged populations of both states involved in the nonadiabatic coupling, explaining the $R > R_0$ region of figure 5.

Using a two-state model, the probability for transition between the two coupled states during one 'sweep' through the zero of the laser field can be calculated [16]. Near the peak of the laser envelope, where the nonadiabatic transitions are the strongest, the transition probability is given by

$$P_{\text{trans}}(R) = \exp\left[\frac{\pi \Delta E_{12}^2(R)}{4\omega V_0(R)}\right], \tag{23}$$

where $\Delta E_{12}(R) = E_1^{(I)} - E_0^{(I)}$ is the bond-dependent field-free energy difference between the two coupled ionic states, $V_0(R) = \mu(R)F_0$ is the strength of the laser coupling and $\mu(R)$ is the bond-dependent transition dipole between the two states. For the present two-center model, we can use the charge-resonance approximation for the ionic transition dipole $\mu(R) \approx R/2$. Figure 5(b) plots $P_{\text{trans}}(R)$ over the range of bond lengths considered, demonstrating that the behavioral change in the dynamics occurring at R_0 is indeed triggered by the onset of nonadiabatic transitions related to electron localization [16].

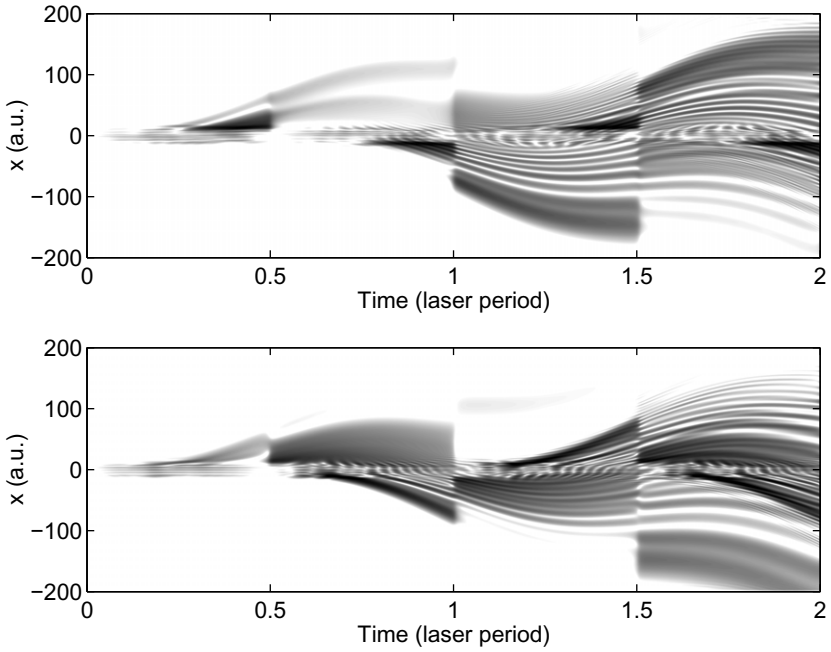

Figure 6. Sub-cycle dynamics of the continuum functions $|\chi_0(x_1, t)|^2$ (top) and $|\chi_1(x_1, t)|^2$ (bottom) correlated to the ground and first excited ionic states, respectively. Bond length $R = 6$ a.u. These plots demonstrated the nonadiabatic ionic transitions that occur near the zeros of the driving laser field.

The nonadiabatic transitions associated with electron localization occur on a sub-cycle timescale and, hence, will influence both the SFI leading to ATI spectra and the HHG emission. Figure 6 shows plots of the time-dependent continuum functions $|\chi_0(x_1, t)|^2$ and $|\chi_m(x_1, t)|^2$ for $R = 6$ a.u. These plots show the behavior of the continuum electron during SFI, analogous to figure 4(a). At each zero of the field there is a sudden 'jump' or 'switching' of the wavefunction. As discussed above, at the zeros of the laser field the ionic state is undergoing a rapid laser-driven nonadiabatic transition, thus causing the continuum electron that ionized initially to, say, the ground ionic state during one half-cycle to find itself on the first excited ionic state during the next half-cycle after the ionic transition occurred.

The dynamics observed in the ion are relevant for ATI and HHG since electron localization causes the ionic state to switch on sub-cycle timescales as the ATI photoelectrons are leaving the core. Thus the ionized population is distributed over both the coupled ionic states. Furthermore, this mechanism explains why the two series of ATI combs do not separate cleanly when measured in coincidence with the ionic state at a large bond length. The nonadiabatic coupling mixes the ionic states on sub-cycle timescales as the ATI electron is leaving the core, and thus the ATI electrons carry signatures of both ionization potentials, resulting in a mixed ATI comb. This point can be generalized beyond simple electron localization. Strong sub-cycle laser-driven nonadiabatic coupling of *any* non-degenerate bound states will result in overlapping ATI combs that cannot be separated by ionic-channel-resolved coincidence measurements. This provides a novel approach to detecting strong laser-driven sub-cycle coupling present during strong-field processes through channel-resolved detection of ATI combs.

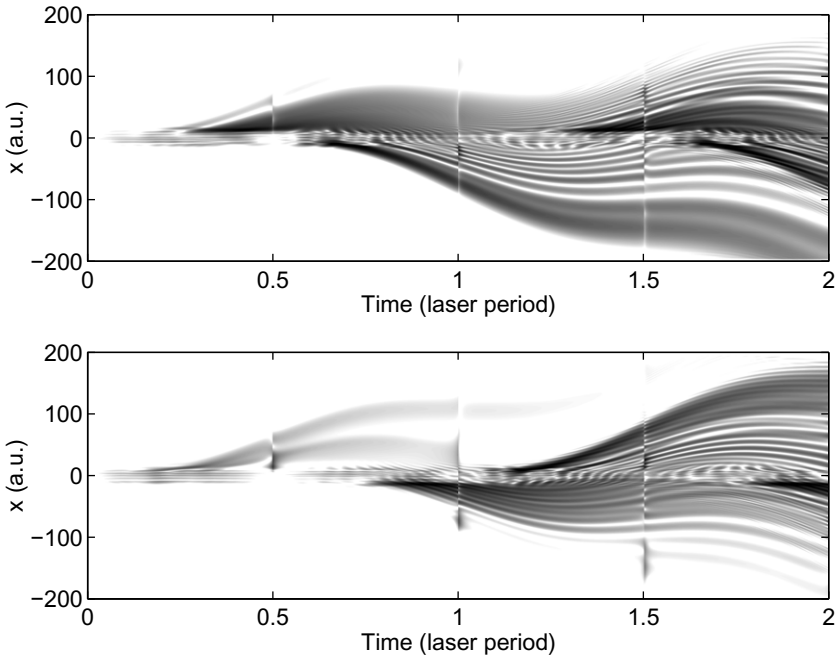

Figure 7. The same as figure 6, but with each half-cycle swapped.

To further strengthen the point that it is the underlying ionic state that is undergoing transitions, figure 7 shows the same wavefunction plots as those in figure 6, but with every second half-cycle swapped. What results is continuous wavefunctions as opposed to the wavefunctions plagued by truncated jumps seen in figure 6. This also suggests that instead of the adiabatically dressed-state basis defined above, one should use a localized basis, where the eigenstates are localized on either the right or left nucleus. Then in this localized basis, the continuum functions would appear continuous as in figure 7. Although this localized basis would be more suitable for large bond lengths, where electron localization is most pronounced ($R > R_0$), it would not be natural for small bond lengths where localization does not occur ($R < R_0$). Thus there will never be a single basis 'qualitatively best suited' to cover a whole range of bond lengths. In addition, neither the localized nor the adiabatic dressed-state basis will fully capture the dynamics in the intermediate bond length regime ($R \approx R_0$) using a single-state description. Here, a coupled multi-state description (in either basis) will always be necessary.

3.4. Reflection of multiple ionic states in the HHG spectra

The participation of multiple ionic states during SFI has consequences not only for the ATI photoelectrons, but also for the emitted HHG spectrum [3–5]. We now consider how the multiple participating ionic states affect the HHG emission for the present model. Figure 8 shows the bond length dependence of the 29th harmonic. Note that there is nothing special about the 29th harmonic. It is simply chosen as an example and any other harmonic shows qualitatively the same behavior. The plot shows the total yield and corresponding phase of the 29th harmonic (thick solid line) calculated from the full wavefunction $\Psi(x_1, x_2, t)$, as well as the harmonic yield from the ground (thin solid) and first excited (dashed) ionic channels calculated using $\Psi^{\mathrm{ex}}(x_1, x_2, t)$ and the dipoles $\mathrm{d}_{00}^{\mathrm{ex}}(t)$ and $\mathrm{d}_{01}^{\mathrm{ex}}(t)$ defined above. We have checked that the coherent

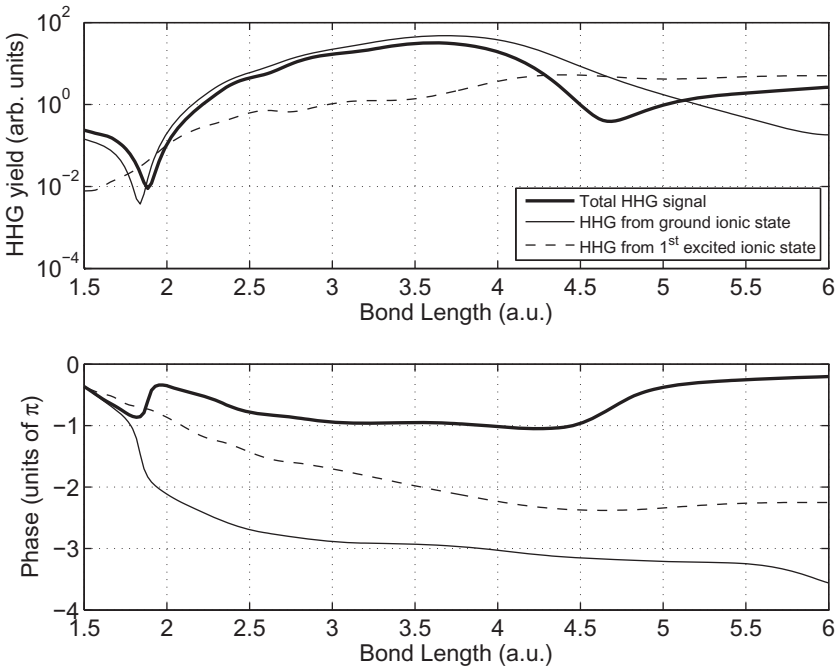

Figure 8. Yield (top) and corresponding phase (bottom) of the 29th harmonic as a function of bond length. Shown are the total yields and phases calculated using the full wavefunction $\Psi(x_1, x_2, t)$, as well as the channel-resolved yields calculated using the wavefunction expansion $\Psi^{\mathrm{ex}}(x_1, x_2, t)$.

sum of the harmonic yield from the ground and first excited ionic channels agrees with the total yield.

Two minima as a function of bond length can be seen in the full harmonic yield, the first around $R_1 = 1.9$ a.u. and the second around $R_2 = 5$ a.u. The first minimum around R_1 is seen to correspond to a minimum present only in the ground ionic channel. No structure is seen near $R = 1.9$ a.u. in the excited ionic state channel. The R_1 minimum thus corresponds to a structural minimum present in the ground ionic channel and is, in fact, a two-center-type minimum [14] present in the ground state HHG channel due to the two-center nature of our model system. The presence of the first excited ionic channel in the HHG emission modifies the appearance of the structural minimum as seen in the total HHG spectrum. In the present model, the structural minimum in the total HHG spectrum is seen to be shifted to slightly higher bond lengths as compared to its position in the ground state channel spectrum. Such effects of multiple participating ionic states on two-center minima in HHG emission have been considered in [7].

Consider now R_2. No minima in the channel-resolved harmonic yields are seen to appear near R_2. Thus, this second minimum is a result of interference between the two participating ionic channels. Further, unlike the two-channel interference for CO_2 discussed in [5] that was due to direct ionization to two ionic states, our two-channel interference arises due to nonadiabatic coupling of two ionic states and is mechanistically similar to the sub-cycle coupling of ionic states in N_2, outlined in [9].

The underlying mechanism for populating the two participating ionic channels near $R_2 = 5$ a.u. has been shown to be related to electron localization (see above). The character of the two ionic states is a localized electron in either the left or the right well. From this perspective, the minima seen near R_2 are also a two-center interference, but now the two-center character arises due to the localized nature of the ionic states, forcing ionization from either the left or right well on subsequent half-cycles. This is opposed to the two-center character appearing with a single channel, as is the case for the R_1 minimum: near R_2, the two-center character appears as a result of multiple ionic states.

4. Summary and outlook

We have explored the effects of multiple final ion states in ATI photoelectron and high-harmonic spectra using a two-center two-electron reduced-dimensionality model. In particular, we demonstrate that ATI photoelectron spectra can be used to directly observe excited ionic populations that result from SFI, a process that is of growing interest to strong field science and attosecond science [3–6].

We proposed and explored ATI probing of a model dissociation scenario showing that the relative yields of the multiple ATI photoelectron combs can signal and track qualitative changes in the ionic excitation mechanism (figure 3). At small bond lengths, where the ATI yield to the ground state of the ion dominates, excited ionic states are predominantly accessed via collisional excitation. At larger bond lengths, where the ATI yields to the ground and first excited states are essentially equal, the route to ionic excitation was primarily through nonadiabatic sub-cycle laser-driven coupling (NME) of the ionic states related to electron localization. This latter case of strong nonadiabatic sub-cycle coupling can be identified in the ATI spectra through ionic-channel-resolved measurements: when strong sub-cycle ionic coupling occurs, the two series of ATI combs seen in the total ATI yield cannot be separated by ionic-channel-resolved ATI measurements, as seen in figures 2(c) and (d) for $R > R_0$. We demonstrate that the multiple participating ionic states identified from the ATI spectra have an effect on the high-harmonic emission. The position and visibility of structural minima may be affected [7], and interferences in the HHG spectrum can arise due to the underlying presence of nonadiabatic laser-driven couplings in the ion [8].

From these results, several outlooks arise. Firstly, it is interesting to see clear evidence for multiple final ionic states participating in SFI, especially considering the simplicity of the present system. This has direct consequences for probing schemes based on HHG, where SFI is the first step. If multiple final ionic states play a non-negligible role in SFI for a system as simple as the present 1D two-electron model, we can expect such processes to occur commonly in real molecules. Indeed, as has been discussed in recent papers [3–5], signatures of multiple final ionic states have been seen in HHG experiments on N_2, CO_2 and $(NO_2)_2$. Consideration of multiple final ionic states during strong field processes will become commonplace as experiments on molecules in strong fields become more sophisticated and the molecules enter the polyatomic (three or more atoms) regime [11].

Second, these results suggest and support the idea of using ATI electrons as a probe of SFI to multiple final ionic states. At the lowest level of sophistication, seeing multiple ATI combs in experiments would immediately give direct evidence for SFI to multiple final ion states, and can also give information about the relative yield of each final ion channel. Further, as has been mimicked in the calculations of figure 2, the ATI spectra can be used to follow

dynamics if a vibration wave packet has been prepared in the target. In this case, the ATI spectra can be used as a secondary probe to test the interpretations of HHG spectra based on multiple participating final ion states. For example, the recent experiment [3] on vibrationally excited $(NO_2)_2$ attributed modulations in the HHG spectra to a change in the relative yield to different final ion states at the inner and outer turning points of the vibrational wave packet. This can be directly confirmed by looking for a corresponding multiple comb structure in the ATI spectra. We believe that channel-resolved ATI spectra will reveal further details of SFI mechanisms in molecules, particularly those undergoing dynamics. As such, they will play an important role in advancing strong field science and attosecond science toward the world of polyatomic molecules.

References

[1] Scrinzi A, Ivanov M Yu, Kienberger R and Villeneuve D M 2006 *J. Phys. B: At. Mol. Opt. Phys.* **39** R1
Lein M 2007 *J. Phys. B: At. Mol. Opt. Phys.* **40** R135

[2] Corkum P B 1993 *Phys. Rev. Lett.* **71** 1994
Lewenstein M, Balcou Ph, Ivanov M Yu, Huillier A L and Corkum P B 1994 *Phys. Rev.* A **49** 2117

[3] Li W, Zhou X, Lock R, Patchkovskii S, Stolow A, Kapteyn H C and Murnane M M 2008 *Science* 1207

[4] McFarland B K, Farrell J P, Bucksbaum P H and Gühr M 2008 *Science* **322** 1232

[5] Smirnova O, Mairesse Y, Patchkovskii S, Dudovich N, Villeneuve D, Corkum P and Ivanov M Yu 2009 *Nature* **460** 972

[6] Akagi H, Otobe T, Staudte A, Shiner A, Turner F, Dörner R, Villeneuve D M and Corkum P B 2009 *Science* **325** 1364

[7] Sukiasyan S, McDonald C, Destefani C, Ivanov M Yu and Brabec T 2009 *Phys. Rev. Lett.* **102** 223002

[8] Lezius M, Blanchet V, Rayner D M, Villeneuve D M, Stolow A and Ivanov M Yu 2001 *Phys. Rev. Lett.* **86** 51
Lezius M, Blanchet V, Ivanov M Yu and Stolow A 2002 *J. Chem. Phys.* **117** 1575

[9] Mairesse Y *et al* 2010 *Phys. Rev. Lett.* **104** 213601

[10] Freeman R R and Bucksbaum P H 1991 *J. Phys. B: At. Mol. Opt. Phys.* **24** 325
DiMauro L F and Agostini P 1995 *Adv. At. Mol. Opt. Phys.* **35** 79

[11] Gijsbertsen A, Boguslavskiy A E, Mikosch J, Spanner M, Patchkovskii S, Gador N, Vrakking M J J and Stolow A 2011 submitted

[12] Javanainen J, Eberly J H and Su Q 1988 *Phys. Rev.* A **38** 3430
Su Q and Eberly J H 1991 *Phys. Rev.* A **44** 5997
Grobe R and Eberly J H 1992 *Phys. Rev. Lett.* **68** 2905

[13] Burnett K, Reed V C, Cooper J and Knight P L 1992 *Phys. Rev.* A **45** 3347

[14] Lein M, Hay N, Velotta R, Marangos J P and Knight P L 2002 *Phys. Rev. Lett.* **88** 183903

[15] Seideman T, Ivanov M Yu and Corkum P B 1995 *Phys. Rev. Lett.* **75** 2819
Sansone G *et al* 2010 *Nature* **465** 763

[16] Dietrich P, Ivanov M Yu, Ilkov F A and Corkum P B 1996 *Phys. Rev. Lett.* **77** 4150